Exciton localization and transfer in azobenzene aggregates: A surface hopping molecular dynamics study

Evgenii Titov*

University of Potsdam, Institute of Chemistry, Theoretical Chemistry, Karl-Liebknecht-Straße 24-25, 14476 Potsdam, Germany

*titov@uni-potsdam.de

Abstract

Molecular photoswitches are a promising class of molecules for development of new functional, light-controlled materials. In complex systems, composed of multiple photoswitchable units, photophysical and photochemical properties may be altered as compared to isolated chromophores. And phenomena such as excitation energy transfer may arise in the aggregated state. In the present work, using nonadiabatic molecular dynamics simulations in conjunction with transition density matrix analysis, we study exciton dynamics in H-type tetramers of azobenzene, a prototypical molecular switch. We consider "free" and "constrained" (embedded in an environment of additional azobenzene molecules) models with different intermolecular distances (3.5 and 5.5 Å). Our simulations reveal ultrafast exciton localization upon $\pi\pi^*$ excitation, occurring on a sub-100 fs timescale, and proceeding faster for the longer separation distance than for the shorter one. We also find that exciton transfer takes place during excited state dynamics in the $\pi\pi^*$ manifold but it is strongly inhibited in the $n\pi^*$ manifold. Moreover, we find that the $\pi\pi^*$ *trans*→*cis* isomerization quantum yields are lower by a factor of about three for free / not strongly constrained tetramers than for the monomer, and no switching is observed for the most tightly packed model.

Introduction

Molecular photoswitches, of which azobenzene is a fundamental example,[1–3] hold promise for developing novel functional materials controlled by light.[4–6] In complex systems, however, numerous photoswitchable units may be present together in a relatively small space volume, and resulting intermolecular interactions between chromophores may affect their photophysics and photochemistry. Examples are azobenzene-functionalized self-assembled monolayers (SAMs),[7–10] micelles,[11–13] surfactant–polymer aggregates,[14–16] and crystalline

systems.[17–19] The aggregation / congestion of azobenzene chromophores in such systems leads to changes in light absorption[13] and emission[17] properties in comparison to "isolated" switches (*e.g.*, in a solution), and, moreover, may hinder or suppress photoisomerization, as has been observed for tightly packed SAMs.[7]

Assembling multiple chromophores together leads to a formation of collective electronic states, known as molecular excitons.[20,21] These states dictate photophysical and photochemical processes in molecular aggregates. Moreover, tight molecular packing induces steric hindrance. Two effects, steric and excitonic, are intrinsically connected, since both become stronger with decreasing intermolecular distances and thus are enhanced at large packing densities. And both effects were proposed to be responsible for hindering azobenzene isomerization in SAMs.[7,22] Furthermore, quantum chemical calculations on azobenzene dimers and larger aggregates yielded sizable exciton splittings (of several hundreds meV) for the bright, $\pi\pi^*$ states, suggesting rapid excitation energy transfer between monomers.[23–26]

The simplest theoretical modelling of the steric effects on photodynamics of a photoswitch requires a quantum mechanical (QM) description of a *single* chromophore, whereas an environment can be described with classical molecular mechanics (MM). This approach has been applied to reveal the role of steric hindrance for azobenzene isomerization in various systems, such as azobenzene (or its derivatives) on a surface,[27,28] in a SAM,[29] attached to RNA,[30] in a micelle,[13] and in a lipid membrane.[31]

The account of the excitonic effects, on the other hand, requires the QM treatment of *multiple* chromophores, and therefore presents a challenge. Benassi and Corni calculated electronic couplings in azobenzene-containing SAMs and modelled exciton diffusion as well as isomerization based on a kinetic model.[32] They concluded that the exciton transfer should not inhibit isomerization in SAMs. In our earlier works, we used a minimal QM azobenzene *dimer* model to study a possible role of the exciton coupling for azobenzene photoisomerization *dynamics*.[33,34] These studies highlighted the dominance of the steric hindrance in reducing quantum yield of the *trans*→*cis* azobenzene isomerization in a tightly packed aggregate. However, the questions of exciton dynamics, localization and transfer have not been addressed at that stage and, moreover, the dimer model may seem too small for exploration of these questions.

Very recently, we studied how ground-state conformation disorder induced by thermal fluctuations affects exciton states of an azobenzene H-type *tetramer* model.[35] It was found that the $\pi\pi^*$ excitons undergo a partial localization, whereas the $n\pi^*$ excitons are strongly localized by disorder.

In the present paper, we perform nonadiabatic, surface hopping molecular dynamics simulations for QM *tetramer* models (with and without additional steric constraint of surrounding MM molecules; and for short and longer intermolecular separation distances) to reveal the fate of the excitons after photoexcitation. We explore the exciton dynamics using a transition density matrix analysis, allowing one to judge on spatial localization of excitons during dynamics.[36–44] In the present study, we treat the electronic subsystem of the tetramers fully quantum mechanically (albeit on a semiempirical level described in the next section), without resorting to more approximate descriptions, such as exciton models.

Very recently, Sangiogo Gil *et al.* developed an exciton model / surface hopping approach within a semiempirical framework.[45] This method has then been applied to an azobenzene-containing SAM model including *twelve* chromophores in the QM region.[46] The central result of Ref. 46 is the absense of exciton transfer between azobenzenes in the $n\pi^*$ manifold and, thus, its unimportance for quenching isomerization. In our present work, we also come to a similar conclusion, and in what follows we will compare our results to the results of Ref. 46 where applicable.

Models and Methods

The models studied in this work are shown in Figure 1.

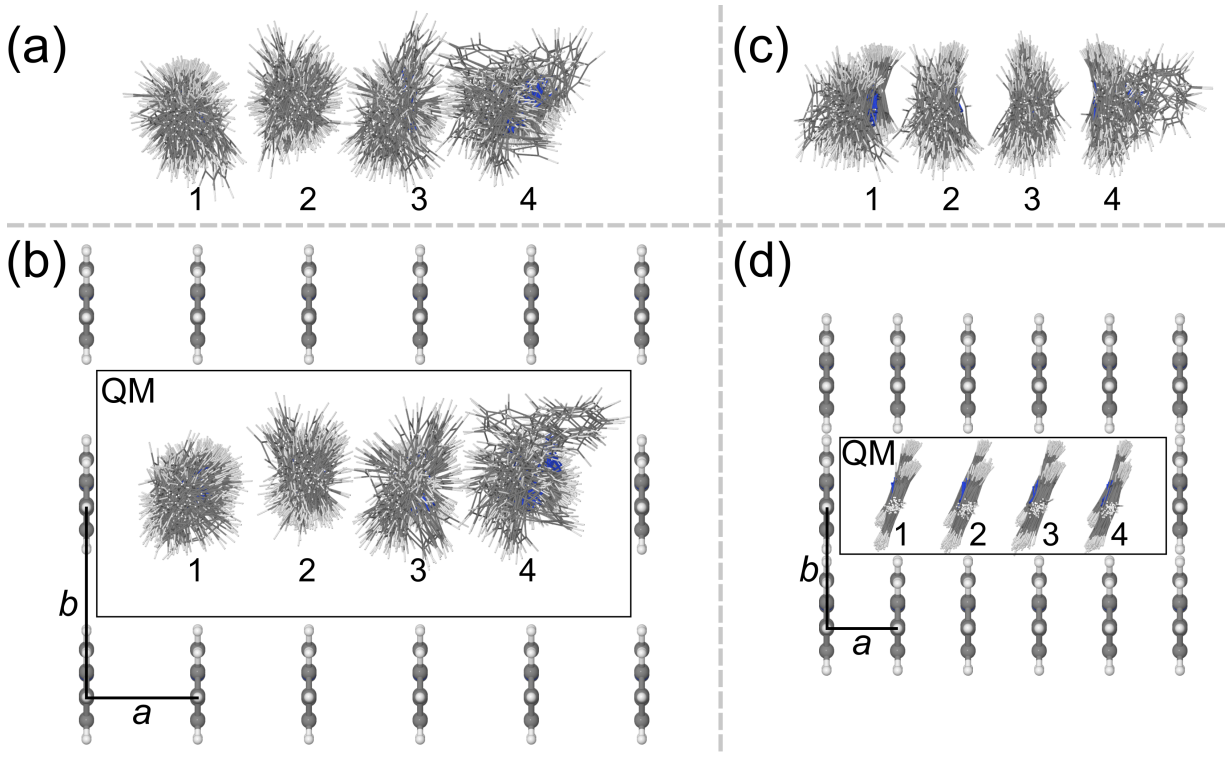

Figure 1: Top view of studied tetrameric models: (a) tetramer 5.5 Å, (b) SAM 5.5 Å, (c) tetramer 3.5 Å, and (d) SAM 3.5 Å. Shown are snapshots (76 for each system) selected from ground-state Langevin MD trajectories (these snapshots are initial geometries for surface hopping trajectories). The QM parts are marked in (b) and (d). The lattice parameters are $a = 5.50$ Å and $b = 9.43$ Å for (b) and $a = 3.50$ Å and $b = 6.00$ Å for (d). The molecule numbering is also shown.

We considered "free" tetramers of stacked azobenzenes with intermolecular separation distances of 5.5 Å (Figure 1a) and 3.5 Å (Figure 1c), as well as "constrained" tetramers, surrounded by additional azobenzene molecules, reminiscent of SAMs (Figure 1b and d,

respectively). The lattice parameters are $a = 5.50$ Å and $b = 9.43$ Å in Figure 1b, and $a = 3.50$ Å and $b = 6.00$ Å in Figure 1d (the a/b ratio is the same in both cases, $a/b \approx 0.583$). For the SAM models, we used a quantum mechanics/molecular mechanics (QM/MM) approach, treating the central tetramer with QM and the perimeter molecules with MM.

The electronic structure of the QM tetramers was modeled with the rAM1/FOMO-CIS method. The method is configuration interaction singles (CIS) based on molecular orbitals (MO) obtained from a self-consistent field calculation with floating occupation (FO) numbers[47] using the Austin Model 1 (AM1)[48] that was reparameterized (r) for azobenzene.[49] For the CIS calculations a restricted active space of eight highest occupied and four lowest virtual orbitals was used. This active space includes orbitals originating from HOMO−1 (π), HOMO (n) and LUMO (π^*) of a monomer (see Figure S1), and it was found to yield satisfactory absorption spectra (see the next section). [HOMO is the highest occupied molecular orbital and LUMO is the lowest unoccupied (virtual) molecular orbital.] In total, 65 Slater determinants are used to construct electronic wave functions.

In addition, to better describe noncovalent interactions, we have added van der Waals (vdW) interaction terms, described with the Lennard-Jones potential, between atoms of different monomers (3456 pairwise potentials in total, for the QM part).[50] The atomic vdW parameters were taken from the OPLS-AA force field.[51] The parameters for atom pairs were calculated taking a geometric mean of the atomic parameters. The used atomic parameters are $\sigma_{\mathrm{C}} = 3.55$ Å, $\sigma_{\mathrm{H}} = 2.42$ Å, $\sigma_{\mathrm{N}} = 3.25$ Å, $\epsilon_{\mathrm{C}} = 0.07$ kcal/mol, $\epsilon_{\mathrm{H}} = 0.03$ kcal/mol, $\epsilon_{\mathrm{N}} = 0.17$ kcal/mol. The MM part of the SAM models interacts with the QM part by the same vdW interaction and the MM molecules were kept fixed during molecular dynamics (MD) simulations. In addition, for the QM tetramer, the C and H atoms closest to an (imaginary) surface (two per monomer) were kept fixed, as in our previous works.[33,34]

Ground-state Langevin MD simulations (on the S_0 rAM1/FOMO-CIS potential energy surface (PES)) were performed to equilibrate the studied systems at $T = 300$ K. The dynamics were run for 20 ps with a time step of 0.2 fs. For each system, the geometries and velocities were selected from the ground-state trajectories every 200 fs, starting at 5 ps, which results in 76 initial conditions (for surface hopping dynamics simulations) per system. These selected, initial geometries are shown in Figure 1.

The vertical electronic spectra were then calculated for the selected geometries using rAM1/FOMO-CIS and the obtained stick spectra were broadened as:

$$I(E) = \frac{1}{N_{sn}} \sum_{\alpha=1}^{N_{sn}} \sum_{i=1}^{N_{st}} f_{i,\alpha} \exp\left(-\frac{1}{2\gamma^2}\left(E - E_{i,\alpha}\right)^2\right) \tag{1}$$

Here, I is intensity, E is excitation energy, $N_{sn} = 76$ is the number of selected snapshots, $N_{st} = 20$ is the number of excited singlet states, $E_{i,\alpha}$ and $f_{i,\alpha}$ are the excitation energy and oscillator strength, respectively, for the $S_0 \rightarrow S_i$ transition, for snapshot α, and $\gamma = 0.18598$ eV (1500 cm^{-1}) is a broadening parameter. The brightest state among the calculated ones was selected as the initial state for the surface hopping calculations. The initial states are of $\pi\pi^*$ character.

The nonadiabatic dynamics were modeled using the trajectory surface hopping ap-

proach[52] combined with the semiempirical configuration interaction method (rAM1/FOMO-CIS in the present study).[53] The SH trajectories were propagated for 10 ps with a time step of 0.1 fs. The energy-based decoherence correction was used to remedy overcoherence of the original surface hopping algorithm.[54] The time-dependent electronic wave function was propagated using the local diabatization scheme,[36,53] which allows one to correctly account for trivial crossings. The nuclei were propagated classically on the on-the-fly calculated adiabatic rAM1/FOMO-CIS PESs. Thirteen lowest singlet states (S_0–S_{12}) were included in the SH simulations.

In all MD simulations we used the so-called added potential (added to each of the four molecules of the tetramer) which corrects the low AM1 inversion barriers and phenyl rotations about the N–C bonds.[49] We note, however, that the state-specific corrections developed in Ref. 49 were not used, since they were derived specifically for monomeric adiabatic states.

Adiabatic electronic state populations were computed as fractions of trajectories being in the state of interest. The quantum yield Φ was computed as the ratio of the number of the reactive trajectories (*i.e.* those undergoing *trans*→*cis* isomerization) to the number N_t of trajectories that reached the ground state within 10 ps. The standard error was calculated as the standard deviation of the sample proportion, $\Delta\Phi = \sqrt{\Phi(1-\Phi)/N_t}$. The reactive trajectories were identified monitoring the change in the CNNC dihedral angles from ∼180° to ∼0°.

The exciton dynamics were traced using the reduced one-particle spinless transition density matrix (TDM) which is defined as:[55]

$$\rho^{0I}(\vec{r},\vec{r}') = N \iint\cdots\int \left[\Psi^0(\vec{x},\vec{x}_2,\ldots,\vec{x}_N)\Psi^I(\vec{x}',\vec{x}_2,\ldots,\vec{x}_N)\right]_{\sigma'\to\sigma} d\vec{x}_2\ldots d\vec{x}_N d\sigma \qquad (2)$$

Here, Ψ^0 is the ground state electronic wave function and Ψ^I is the excited current state electronic wave function, $\vec{x}$ collects spatial $\vec{r}$ and spin σ variables of an electron, and N is the number of electrons. We note that the electronic wave functions depend parametrically on the nuclear coordinates $\mathbf{R}(t)$ (which, in turn, depend on time in quantum–classical trajectory-based methods), but we do not write explicitly this dependence for the sake of brevity. We also assume the wave functions to be real.

The electronic, adiabatic wave functions are linear combinations of the unexcited and singly-excited Slater determinants Φ_K:

$$\Psi^{0/I}(\mathbf{x}) = \sum_K C_K^{0/I}\Phi_K(\mathbf{x}) \qquad (3)$$

Here, $\mathbf{x}$ collects the variables of all electrons.

Substitutig Equation (3) into Equation (2), one can rewrite the TDM as an expansion in MO products, and further expressing MOs φ_i as linear combinations of atomic orbitals (AOs) η_μ, $\varphi_i(\vec{r}) = \sum_\mu c_{\mu i}\eta_\mu(\vec{r})$, as an expansion in AO products:

$$\begin{aligned}\rho(\vec{r},\vec{r}') &= N\sum_{K,L} C_K^0 C_L^I \iint\cdots\int [\Phi_K\Phi_L]_{\sigma'\to\sigma}\, d\vec{x}_2\ldots d\vec{x}_N d\sigma \\ &= \sum_{i,j} P_{ij}^{[\mathrm{MO}]}\varphi_i(\vec{r})\varphi_j(\vec{r}') \\ &= \sum_{\mu,\nu} P_{\mu\nu}^{[\mathrm{AO}]}\eta_\mu(\vec{r})\eta_\nu(\vec{r}')\end{aligned} \tag{4}$$

Here, $\mathbf{P}^{[\mathrm{MO}]}$ and $\mathbf{P}^{[\mathrm{AO}]}$ are TDMs in MO and AO basis, respectively. In our case, the $\mathbf{P}^{[\mathrm{MO}]}$ matrix has a size of 12×12, and the $\mathbf{P}^{[\mathrm{AO}]}$ matrix 264×264.

Further, we contract the $\mathbf{P}^{[\mathrm{AO}]}$ matrix to monomers[56,57] (denoted with X, Y) by computing the "fraction of transition density matrix" (FTDM) matrix $\mathbf{F}$:[58]

$$F_{XY} = \frac{\sum_{\mu\in X}\sum_{\nu\in Y}\left(P_{\mu\nu}^{[\mathrm{AO}]}\right)^2}{\sum_{\mu\in\mathrm{tetramer}}\sum_{\nu\in\mathrm{tetramer}}\left(P_{\mu\nu}^{[\mathrm{AO}]}\right)^2} \tag{5}$$

The diagonal elements F_{XX} quantify contributions of local excitations and off-diagonal elements F_{XY}, $Y \neq X$ charge-transfer excitations. For a tetramer, the $\mathbf{F}$ matrix has a size of 4×4.

Using the elements of the $\mathbf{F}$ matrix, we compute the inverse participation ratio (IPR):[59]

$$\mathrm{IPR} = \frac{1}{\sum_X\left(\sum_Y \frac{F_{XY}+F_{YX}}{2}\right)^2} \tag{6}$$

IPR is a *scalar* ranging from 1 (complete exciton localization) to 4 (complete exciton delocalization). We also compute overall measures of local excitations (LE) and charge transfer (CT) as:

$$\mathrm{LE} = \sum_X F_{XX} \tag{7a}$$

$$\mathrm{CT} = \sum_{X\neq Y} F_{XY} \tag{7b}$$

In addition, we introduce highest (H), intermediate (H−1 and L+1), and lowest (L) monomers through sorting the FTDM diagonal, $F_{\mathrm{H}} > F_{\mathrm{H-1}} > F_{\mathrm{L+1}} > F_{\mathrm{L}}$, allowing one to judge on exciton localization on single geometry level (for excitons dominated by local excitations).[35,40,60] We note that we calculate FTDM and derived quantities (IPR, LE, and CT) along surface hopping trajectories, *i.e.* these quantities depend on $\mathbf{R}(t)$. Finally, averaging over a swarm of trajectories (for a given system) is performed.

To enable a comparison to the monomer dynamics at (approximately) the same level of theory, we performed SH simulations for a single AB molecule using rAM1/FOMO-CIS with a small active space including only HOMO−1, HOMO, and LUMO (see Figure S1),

thus resulting in five Slater determinants to represent the wave functions of the mononer. Three singlet states (S_0, S_1, and S_2) were used in the SH simulations for the monomer. The two atoms in a *para* position (C and H) were fixed, similarly to the tetramer cases.

The rAM1/FOMO-CIS calculations were done with the development version of MOPAC 2002.[61] The TINKER package was used to handle QM/MM interactions.[62]

Results and Discussion

Figure 1 shows the snapshots selected from the ground-state Langevin trajectories. Azobenzene units experience much larger conformational freedom for SAM 5.5 Å (Figure 1b) than for SAM 3.5 Å (Figure 1d). The free tetramer 5.5 Å (Figure 1a) shows a similar spread of geometries to that of SAM 5.5 Å, whereas the free tetramer 3.5 Å (Figure 1c) demonstrates larger geometrical variability than SAM 3.5 Å but lesser than models with $a = 5.5$ Å.

Absorption spectra of the tetrameric models as well as that of the monomer are shown in Figure 2a.

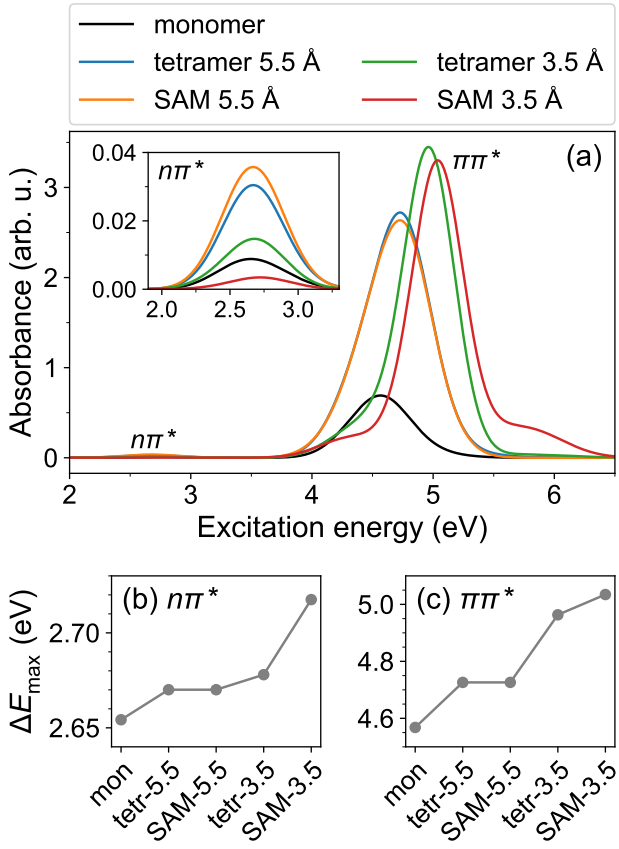

Figure 2: (a) Absorption spectra of the studied systems calculated at the snapshots shown in Figure 1. (b) and (c) Peak positions $\Delta E_{\max}$ for the $n\pi^*$ and $\pi\pi^*$ bands, respectively.

The spectra of all systems show a strong $\pi\pi^*$ band in ultraviolet region and a weak $n\pi^*$ band in the visible region. The peak positions of the $n\pi^*$ and $\pi\pi^*$ bands are plotted in Figure 2b and c, respectively. The $\pi\pi^*$ band of the monomer is located at 4.57 eV. This value is blue-shifted by 0.45 eV with respect to the available gas-phase experimental value of 4.12 eV[63] but is in reasonable agreement with results obtained using time-dependent long-range corrected density functional theory (TD-lc-DFT) in combination with ground-state DFT MD, 4.2–4.6 eV.[35] For the tetrameric models, the $\pi\pi^*$ band is considerably blue-shifted because of exciton coupling (Figure 2a,c). For the models with $a = 5.5$ Å, the blue shift is 0.16 eV, for tetramer 3.5 Å 0.40 eV, and for SAM 3.5 Å 0.47 eV. Moreover, the tetramer absorbance at band maxima is larger than the monomer absorbance (as expected based on the molecular exciton model[21]). Specifically, enhancement factors are 3.9, 3.8, 5.0, 4.8 for tetramer 5.5 Å, SAM 5.5 Å, tetramer 3.5 Å, SAM 3.5 Å, respectively.

For the lower energy $n\pi^*$ band, the monomer peak position is at 2.65 eV, which again is in reasonable aggrement with TD-lc-DFT results (2.5–2.8 eV).[35] The experimental gas-phase peak position is 2.82 eV.[63] The $n\pi^*$ band experiences a much smaller blue shifts when going to the tetrameric models: 0.016 eV for models with $a = 5.5$ Å, 0.024 eV for tetramer 3.5 Å, and 0.063 eV for SAM 3.5 Å (Figure 2b). The intensity of the $n\pi^*$ band is considerably enhanced for loosely packed models ($a = 5.5$ Å), in 3.4 and 4.0 times for tetramer 5.5 Å and SAM 5.5 Å, respectively. However, the enhancement is much smaller for tetramer 3.5 Å (factor of 1.7) and, notably, diminution in absorbance is observed for tightly packed SAM 3.5 Å (factor of 0.4), see inset in Figure 2a. This may be explained by the fact that the transition dipole moment of planar *trans* azobenzene is zero, and larger conformational changes, accessible for the free molecule or not strongly constrained aggregates, tend to increase it.[33,64] We also note that the spectra of free and constrained (SAM) tetramers with $a = 5.5$ Å are very similar to each other, reflecting similarities between the conformationally disorded structural ensembles shown in Figure 1a,b. For $a = 3.5$ Å, spectral and geometrical differences are much larger (see Figure 1c,d and Figure 2a).

Then we modelled nonadiabatic dynamics after excitation to the $\pi\pi^*$ band, starting in the brightest $\pi\pi^*$ state. This state was in most cases S_8 but not always. Namely, it was always S_8 for tetramer 3.5 Å. For SAM 3.5 Å, one trajectory was launched from S_9. For tetramer 5.5 Å, eleven trajectories started in S_7. And for SAM 5.5 Å, 19 trajectories were launched from S_7 and one from S_6. The electronic state populations, grouped in $n\pi^*$ and $\pi\pi^*$ manifolds (plus the ground state), are shown in Figure 3. For the tetrameric models, the $n\pi^*$ manifold includes states S_1–S_4, whereas the $\pi\pi^*$ manifold states S_5–S_{12}. For the monomer, $n\pi^*$ is S_1 and $\pi\pi^*$ is S_2. We fitted population curves as follows:

$$P_{\pi\pi^*} = e^{-t/\tau_{\pi\pi^*}} \tag{8a}$$

$$P_{n\pi^*} = \frac{\tau_{n\pi^*}}{\tau_{n\pi^*} - \tau_{\pi\pi^*}}(e^{-t/\tau_{n\pi^*}} - e^{-t/\tau_{\pi\pi^*}}) \tag{8b}$$

$$P_{S_0} = 1 - e^{-t/\tau_{S_0}} \tag{8c}$$

and the corresponding time constants $\tau_{\pi\pi^*}$, $\tau_{n\pi^*}$ and τ_{S_0} are shown in Table 1. Equations (8a) and (8b) describe a two-step irreversible kinetic model $\pi\pi^* \rightarrow n\pi^* \rightarrow S_0$.

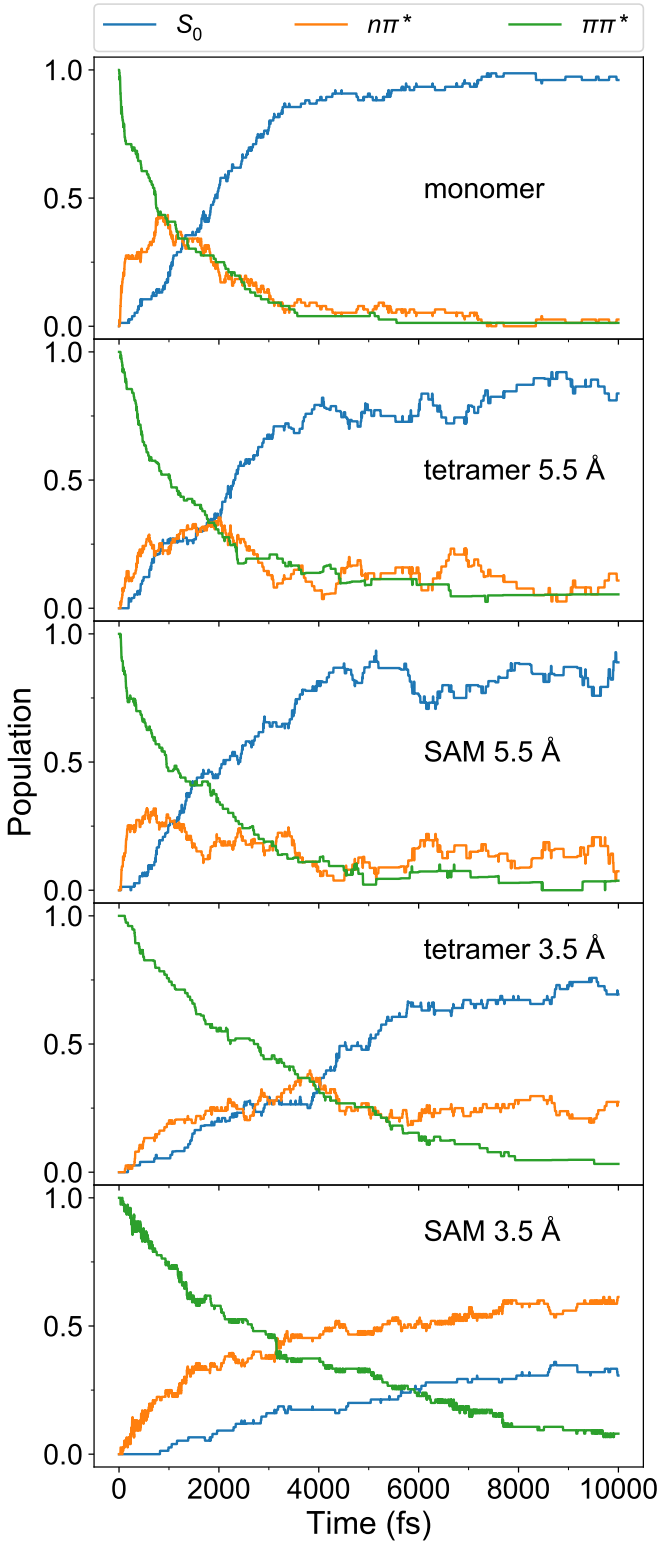

Figure 3: Adiabatic populations of S_0, $n\pi^*$ and $\pi\pi^*$ states for the studied systems.

Table 1: Quantum yields, excited state lifetimes, and exciton localization time constants for the studied systems

System	Φ (%)	$\tau_{\pi\pi^*}$ (fs)	$\tau_{n\pi^*}$ (fs)	τ_{S_0} (fs)	τ_{loc} (fs)
monomer	14.7 ± 4.1	1232	957	2379	—
tetramer 5.5 Å	5.1 ± 2.9	1759	1287	3618	22
SAM 5.5 Å	4.9 ± 2.8	1716	1055	3304	19
tetramer 3.5 Å	4.6 ± 2.6	3392	3022	7382	44
SAM 3.5 Å	0	3847	10751	21736	101

Population dynamics for models with $a = 5.5$ Å are qualitatively similar to those of the monomer. For the latter, we find a $\pi\pi^*$ lifetime of ∼1.2 ps, which is longer than calculated with more sophisticated methods, ∼100–400 fs.[33,65–69] We stress that here, for the monomer, we use rAM1/FOMO-CIS including three orbitals only to enable more direct comparison to results for the tetramers. The $n\pi^*$ lifetime for the monomer is ∼1 ps, which is again slower than reported in other computational works, ∼100–500 fs.[33,66,67] The recovery time of the ground state τ_{S_0} is ∼2.4 ps.

For tetramer 5.5 Å and SAM 5.5 Å, the dynamics are slightly slower: $\tau_{\pi\pi^*} \approx 1.8$ and 1.7 ps, $\tau_{n\pi^*} \approx 1.3$ and 1.1 ps, and $\tau_{S_0} \approx 3.6$ and 3.3 ps, respectively.

For tetramer 3.5 Å and SAM 3.5 Å, the $\pi\pi^*$ lifetimes are longer, ∼3.4 and 3.8 ps, respectively. Inspecting populations of individual states, we observe that the S_5 state (the lowest $\pi\pi^*$ state) is rapidly populated in all cases (Figure S2). However, it is populated slower and also decays slower for models with $a = 3.5$ Å than for models with $a = 5.5$ Å (Figure S2). In this respect, we note that for the dimeric models with $a = 3.5$ Å studied in Ref. 33 the $\pi\pi^*$ lifetime for the SAM was reduced by a factor of 3 with respect to the free dimer. A possible reason for this discrepancy is another electronic structure method used in Ref. 33 (including more orbitals and excitations).

The $n\pi^*$ lifetimes are also prolonged for $a = 3.5$ Å, to ∼3 and ∼11 ps for the free tetramer and SAM, respectively. It is in qualitative agreement with Ref. 33. The corresponding ground-state recovery times are ∼7.4 ps and ∼21.7 ps. Thus, we observe that the return to the ground state is delayed in the tightly packed SAM. It is again in qualitative agreement with previous simulations.[29,33,46]

It is interesting to compare the obtained lifetimes to those reported in the recent study employing exciton model / surface hopping approach, performed for 12 QM azobenzene chromophores.[46] After $\pi\pi^*$ excitation, the following lifetimes were obtained: $\tau_{\pi\pi^*} \approx 0.27$ ps and $\tau_{n\pi^*} \approx 3.41$ ps. Whereas a direct comparison is not possible since the considered systems are different, we note that the $\pi\pi^*$ lifetime of Ref. 46 is much shorter than the $\pi\pi^*$ lifetimes in Table 1. This may originate from the long $\pi\pi^*$ lifetime of the monomer obtained here using the simple, three orbital CIS level.

Further, we computed quantum yields Φ for the *trans*→*cis* isomerization (see Table 1). For the monomer, we find the quantum yield of about 15 %, in good agreement with the available literature values.[66,69,70] For models with $a = 5.5$ Å, the quantum yield is reduced to $\Phi \approx 5$ %, for both free tetramer and SAM. Any of the four QM molecules can be switched for $a = 5.5$ Å. For tetramer 3.5 Å, $\Phi \approx 4.6$ %. In this case, for reactive

trajectories, only end molecules (1 and 4) show isomerization. For SAM 3.5 Å no switching was observed, $\Phi = 0$. We note that for the quantum yield calculations we used only those trajectories that reached the ground state (S_0) within 10 ps.

In our previous work on the dimeric models, we found the following quantum yields: monomer, 21 %; dimer 3.5 Å, 19 %; dimeric SAM 3.5 Å, 11 %; and dimeric SAM 5.5 Å, 22 %.[34] While the main observation of the reduced quantum yield in the densely packed SAM is qualitatively the same, we observe the following quantitative differences. First, in the previous work the quantum yield of the dimer 3.5 Å and SAM 5.5 Å are approximately the same as that for the monomer, but in the present work, for models with $a = 5.5$ Å and for tetramer 3.5 Å, the quantum yields are reduced by a factor of $\sim$3 with respect to the monomer. Second, whereas the quantum yield of the dimeric SAM 3.5 Å is reduced by a factor of $\sim$2 (but still is nonzero), no switching was observed for the tetrameric SAM 3.5 Å studied here. There are several possible reasons for these discrepancies: (i) the QM part is larger in the present work, four instead of two molecules, (ii) electronic structure methods are different in terms of orbital active space size and allowed excitations, (iii) in this work, the additional vdW term is used in the QM part to better describe noncovalent interactions, and (iv) the added potential is applied in the present work in contrast to the previous work.

To analyze this issue, we performed surface hopping simulations for free dimers using the vdW-corrected rAM1/FOMO-CIS method with the active space of four occupied and two virtual orbitals (17 Slater determinants), using the same procedure as for tetrameric systems (76 initial conditions per dimer). For dimer 3.5 Å, we obtain quantum yield $\Phi = 14.3 \pm 4.2$ %. The quantum yield is similar to that of the monomer (14.7 %), in agreement with our earlier report (employing more excitations to describe the electronic structure).[33] For dimer 5.5 Å, we obtain a somewhat smaller quantum yield $\Phi = 9.3 \pm 3.4$ %. Thus, it appears that enlargement of the QM part (from two to four molecules) results in the reduction of the switching probability. Interestingly, this effect is observed not only for the shorter intermolecular distance ($a = 3.5$ Å) but also for the longer one ($a = 5.5$ Å).

Further, using the TDM analysis, we investigated exciton localization and transfer in the studied aggregates. The IPR curves averaged over a swarm of trajectories are shown in Figure 4.

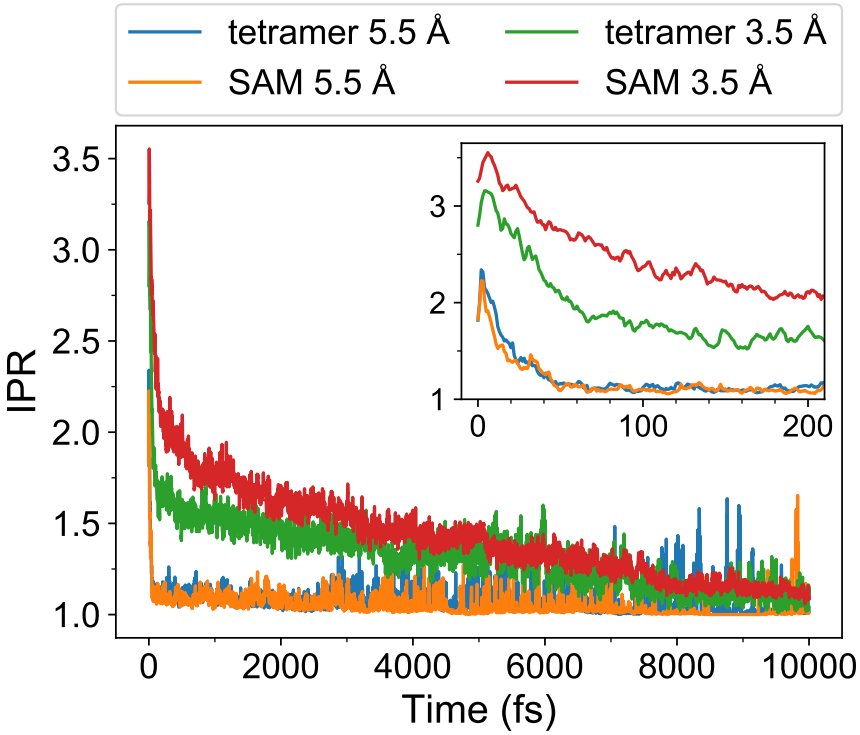

Figure 4: Ensemble-averaged inverse participations ratio (IPR) as a function of time for the studied models. The inset shows the IPR behaviour during first 200 fs of dynamics.

We observe an ultrafast falloff in IPRs, on a fs timescale, for all studied models. This demonstrates the ultrafast exciton localization. In more detail, the initial IPR values are 1.82, 1.83, 2.80, and 3.26 for tetramer 5.5 Å, SAM 5.5 Å, tetramer 3.5 Å, and SAM 3.5 Å, respectively. Thus, the initial exciton is already quite localized for the models with $a = 5.5$ Å, but is more delocalized for the systems with $a = 3.5$ Å. The (partial) localization is the result of thermally induced conformational disorder.[35] There is only a very minor difference in the initial IPR values between tetramer 5.5 Å and SAM 5.5 Å, but the difference between tetramer 3.5 Å and SAM 3.5 Å is much larger, 2.80 vs. 3.26, showing a more delocalized exciton for SAM 3.5 Å. This correlates with the difference in conformational flexibility (see Figure 1). The value for tetramer 3.5 Å, 2.80, is in good agreement with our earlier TD-lc-DFT results, which yielded IPR of about 2.5–3.1.[35]

Further, the IPR curves exhibit an extremely ultrafast initial rise, reaching a maximum at 2 fs, 2 fs, 4 fs, and 6 fs for tetramer 5.5 Å, SAM 5.5 Å, tetramer 3.5 Å, and SAM 3.5 Å, respectively (see the inset in Figure 4). The corresponding IPR maximal values are 2.34, 2.23, 3.16, and 3.55. Thus, directly after the excitation, the exciton becomes more delocalized. Interestingly, a similar behaviour was observed in Ref. 36 for the 2-pyridone dimer. The subsequent excited-state dynamics leads to exciton localization. In order to estimate the localization time τ_{loc}, we fitted the IPR curves using the following functions:

$$\mathrm{IPR} = A\exp(-t/\tau_{\mathrm{loc}}) + C \tag{9a}$$
$$\mathrm{IPR} = A\exp(-t/\tau_{\mathrm{loc}}) + B\exp(-t/\tau) + C \tag{9b}$$

The monoexponential fit Equation (9a) was applied for the models with $a = 5.5$ Å, and the double exponential Equation (9b) was used for the models with $a = 3.5$ Å. For the latter, τ_{loc} describes the fastest decay component. The localization times are collected in the last column of Table 1. For the systems with $a = 5.5$ Å, τ_{loc} is about 20 fs. For tetramer 3.5 Å, $\tau_{\mathrm{loc}} = 44$ fs. And for SAM 3.5 Å, $\tau_{\mathrm{loc}} = 101$ fs. Accordingly, the exciton localization occurs faster for more weakly coupled systems. In addition, the localization times τ_{loc} correlate with the $\pi\pi^*$ lifetimes $\tau_{\pi\pi^*}$ (Table 1). However, a (partial) localization of the $\pi\pi^*$ states occurs before relaxation to the $n\pi^*$ states.

During excited-state dynamics, the $\pi\pi^*$ excitons become more localized for models with $a = 5.5$ Å than for $a = 3.5$ Å, which can be anticipated from Figure 4. To quantify the degree of exciton localization for dynamics in the $\pi\pi^*$ and $n\pi^*$ manifolds, we calculated IPRs for these two manifolds separately, *i.e.* for a given time t averaging was performed only over those trajectories which are in the respective state manifold ($\pi\pi^*$ or $n\pi^*$) at time t. The corresponding IPR curves are shown in Figure 5. For models with $a = 5.5$ Å, the $\pi\pi^*$ IPR curves saturate at IPR ≈ 1.1. For tetramer 3.5 Å, the corresponding saturation value is $\sim$1.6. And for SAM 3.5 Å, it is $\sim$2.0. The $n\pi^*$ IPR curves pass mostly at IPR ≈ 1.0, for all systems, meaning that the $n\pi^*$ excitons are strongly localized for all considered models. Therefore, a slower decrease of overall IPRs at long times for models with $a = 3.5$ Å, corresponding to the second time constant τ in Equation (9b), (see Figure 4) is caused by transitions to the $n\pi^*$ manifold (ultimately to the S_1 state). We also note that the $\pi\pi^*$ IPR curves become more "noisy" at longer times (see Figure 5) because the number of trajectories being in the $\pi\pi^*$ states decreases with time.

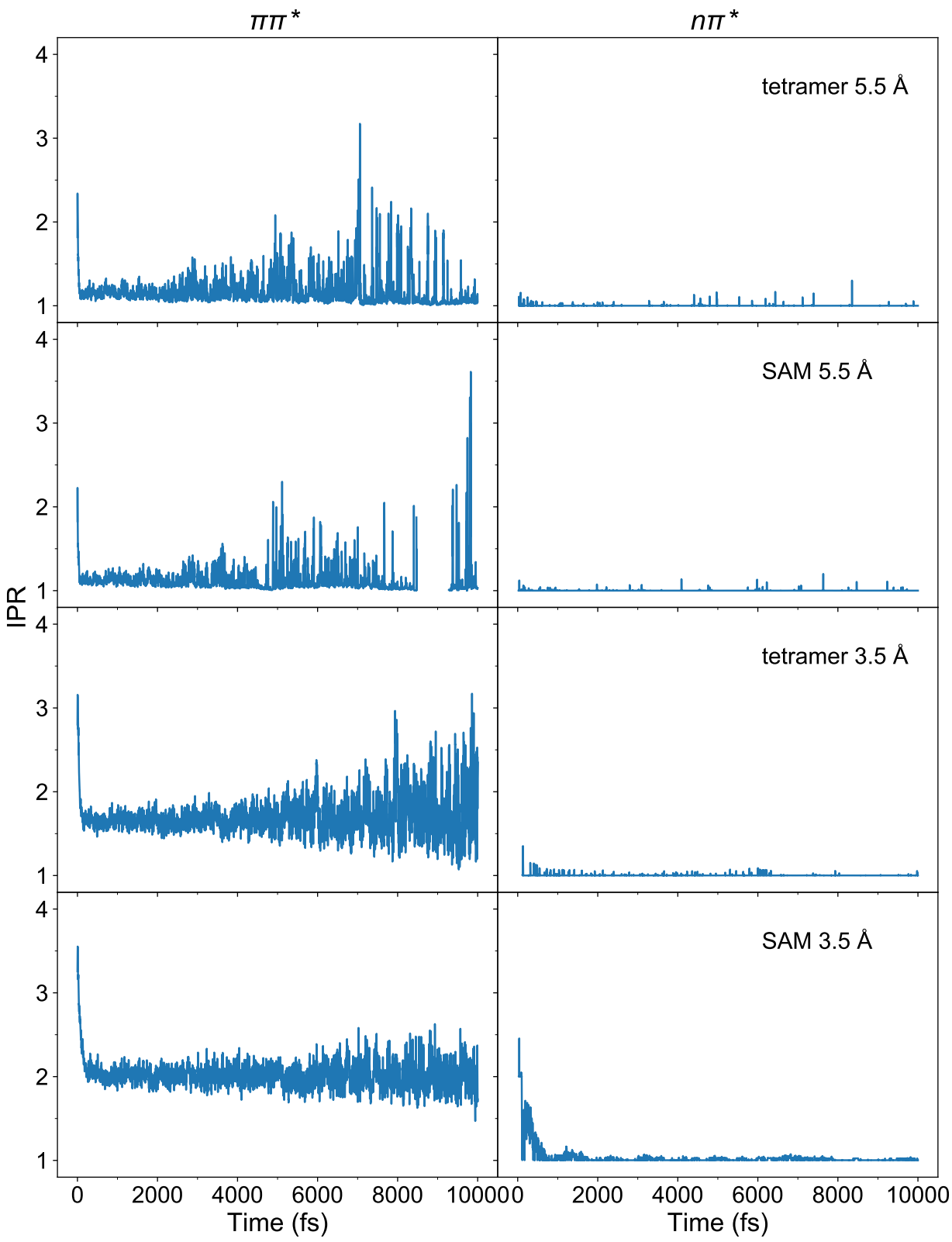

Figure 5: Ensemble-averaged IPRs for $\pi\pi^*$ states (left column) and $n\pi^*$ states (right column), for all tetrameric models.

Further, we calculated the LE and CT measures along the trajectories. These measures averaged over the swarm of trajectories are shown in Figure 6, for SAM 3.5 Å. At time $t = 0$, LE ≈ 0.84 and CT ≈ 0.16. Thus, the initial brightest states contain some nonnegligible admixture of CT excitations (for SAM 3.5 Å). Following photoexcitation, LE slightly decreases and CT increases, reaching after about 10 fs values of 0.75 and 0.25, respectively. After oscillating at this level for 90 fs more, LE starts to increase and CT to decrease, reaching at 10 ps LE ≈ 0.99 and CT ≈ 0.01. For the other studied systems LE ≈ 1 and CT ≈ 0 throughout the dynamics (see Figure S3).

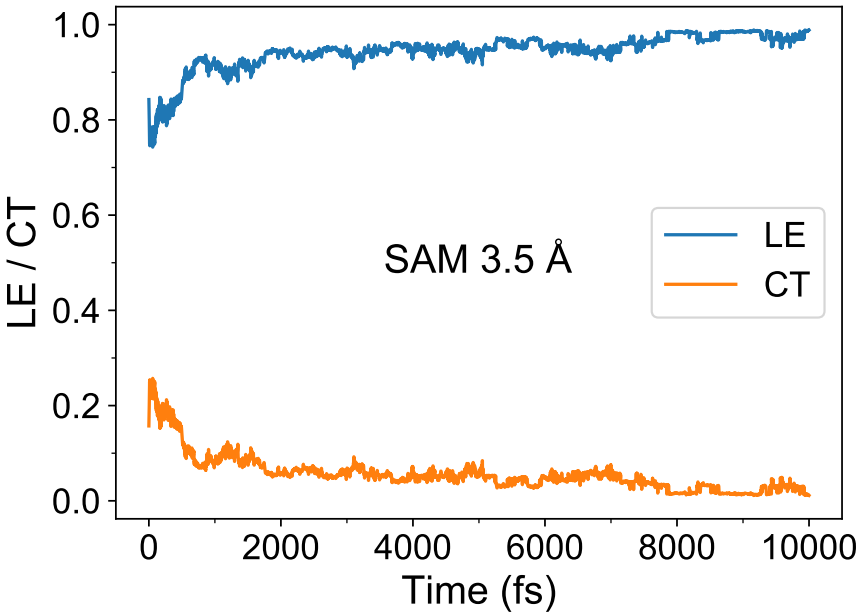

Figure 6: LE and CT measures, averaged over a swarm of trajectories, as a function of time, for SAM 3.5 Å.

In order to deepen insight into the dynamics, we show selected characteristics along single trajectories in Figure 7, for SAM 5.5 Å (left column) and SAM 3.5 Å (right column). The selected characteristics are F_{XX} matrix elements, $F_{\mathrm{H/H-1/L+1/L}}$ values, IPR, CT, and the active electronic state. The areas shaded in grey correspond to being in one of the $n\pi^*$ states.

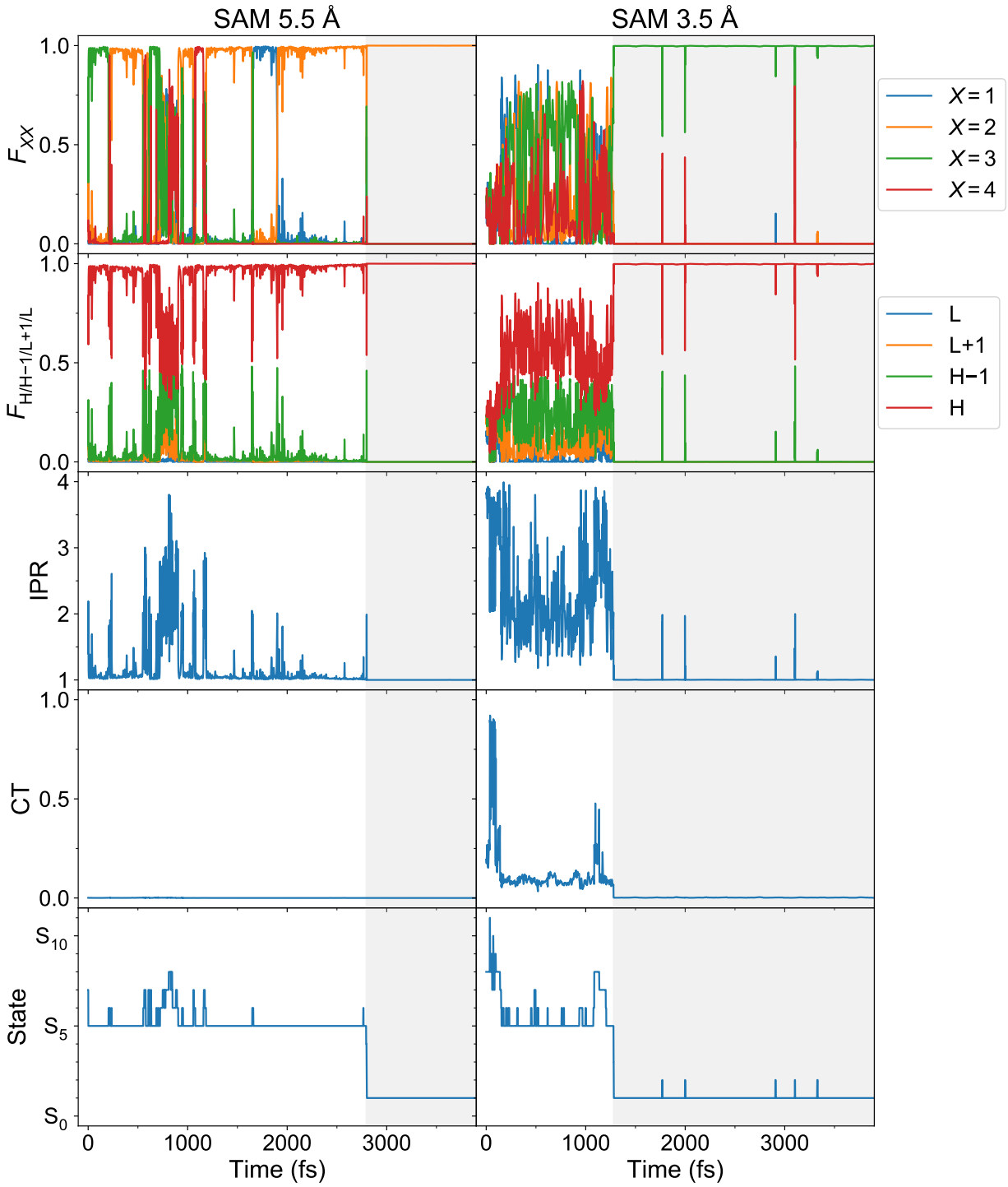

Figure 7: Time-evolution of various quantities of interest for two single trajectories, one for SAM 5.5 Å (left) and the other one for SAM 3.5 Å (right). Shown are, from top to bottom, F_{XX} ($X = 1...4$), highest to lowest FTDM diagonal elements $F_{\mathrm{H/H-1/L+1/L}}$, IPR, CT, and the active electronic state. The areas shaded in grey correspond to being in the $n\pi^*$ manifold.

For SAM 5.5 Å, for the shown trajectory, the exciton rapidly localizes at the third monomer ($X = 3$). Subsequently, the exciton remains mostly localized experiencing sometimes transient delocalization and exciton transfer from one monomer to another, while being in the $\pi\pi^*$ manifold. The transient delocalization can be clearly deduced from the second row, for times at which F_{H} is not close to 1. The single-trajectory IPR (third row) also shows a rapid relaxation to ∼1 but with spikes at times corresponding to the transient delocalization. We note that CT is virtually zero in this case (the fourth row). The transient delocalization and the exciton transfer are sometimes but not always accompanied by nonadiabatic transitions (surface hops) between adiabatic states (compare the three upper rows with the lower row, which shows the active electronic, adiabatic state). For example, the period of relatively lengthy transient delocalization between 720 and 910 fs comes together with the population of higher lying excited states (which are above S_5). Notably, after transition to the $n\pi^*$ manifold, the exciton is strongly localized ($F_{22} = 1$, $F_{\mathrm{H}} = 1$, IPR = 1; FTDM and IPR curves are less noisy than for the $\pi\pi^*$ manifold) and it remains at a single fragment ($X = 2$ for the shown trajectory) without being transferred. This is in agreement with the recent conclusion of Sangiogo Gil *et al.*[46] Importantly, the absence of the exciton transfer in the $n\pi^*$ manifold is observed for almost all trajectories with an exception of two trajectories for tetramer 3.5 Å and two trajectories for SAM 3.5 Å. And for these exceptional trajectories, only a single transfer event takes place per trajectory.

For SAM 3.5 Å, for the presented trajectory (see the right column of Figure 7), the exciton is more delocalized (than for SAM 5.5 Å) while the system resides in the $\pi\pi^*$ states. However, a partial localization is observed during dynamics in the $\pi\pi^*$ manifold (compare to the initial IPR value of ∼3.8 for the given trajectory). The CT contributions are larger for SAM 3.5 Å, and become dominant at some times, *e.g.* CT reaches values of up to 0.9 between 35 and 100 fs. At 35 fs, we also observe an upward surface hop from the initially populated S_8 state to S_{10}, which is accompanied by the change in CT from ∼0.2 to ∼0.9. We also observe an increase in CT up to ∼0.45 at around 1100 fs, which is again associated with upward nonadiabatic transitions (from S_5 in this case). Once the $n\pi^*$ states are populated, the exciton becomes strongly localized (the IPR, F_{H} and F_{33} values are 1), on the third monomer in the presented case ($X = 3$). We also observe spikes in FTDM and IPR curves (while being in the $n\pi^*$ manifold) correlated with surface hops between S_1 and S_2.

Conclusions

We performed nonadiabatic, surface hopping molecular dynamics simulations for H-type azobenzene tetramers to investigate exciton localization and transfer in these aggregates upon $\pi\pi^*$ excitation. Free and constrained (SAM-like) models were considered, with short ($a = 3.5$ Å) and longer ($a = 5.5$ Å) intermolecular, nearest-neighbour distances. The electronic structure of the tetramers were treated at the semiempirical rAM1/FOMO-CIS level, allowing us to afford surface hopping dynamics simulations for the relatively large QM part including four azobenzene molecules. The exciton dynamics were explored using

transition density matrix analysis.

Our simulations reveal ultrafast exciton localization with characteristic time constants of about 20 fs for the models with $a = 5.5$ Å, ∼40 fs for free tetramer with $a = 3.5$ Å, and ∼100 fs for SAM with $a = 3.5$ Å. The exciton localization times are much shorter than the corresponding $\pi\pi^*$ lifetimes, which are on a ps timescale at the used level of theory. During excited state dynamics the $\pi\pi^*$ states undergo a stronger localization for longer intermolecular distances ($a = 5.5$ Å) than for the shorter ones ($a = 3.5$ Å). Moreover, we observe exciton transfer between azobenzene monomers while dynamics proceed in the $\pi\pi^*$ manifold. The $n\pi^*$ excitons are mostly completely localized (on a single monomer). And once the $n\pi^*$ exciton is localized on a particular monomer, it is usually trapped there, whereas exciton transfer to another monomer is a rare event (observed only for four trajectories, in case of models with $a = 3.5$ Å).

We also find that quantum yields of the *trans*→*cis* isomerization induced by $\pi\pi^*$ excitation are lower for tetramers in comparison to the monomer, by a factor of about 3 for all considered models with exception of the tightly packed SAM ($a = 3.5$ Å), for which no isomerization was observed in our simulations.

Acknowledgements

The author is grateful to Giovanni Granucci and Maurizio Persico for providing their surface hopping program. The author is very thankful to Giovanni Granucci for extending the program capabilities to meet the needs of the present study and for valuable discussions. The author is also very thankful to Peter Saalfrank for providing computational resources and for his comments on the manuscript. The author is grateful to the Deutsche Forschungsgemeinschaft (DFG, German Research Foundation) for financial support – project number 454020933. (Gefördert durch die Deutsche Forschungsgemeinschaft (DFG) – Projektnummer 454020933.) The author also acknowledges support by the University of Potsdam.

References

(1) Bandara, H. M. D.; Burdette, S. C. Photoisomerization in different classes of azobenzene. *Chem. Soc. Rev.* **2012**, *41*, 1809–1825.

(2) Beharry, A. A.; Woolley, G. A. Azobenzene photoswitches for biomolecules. *Chem. Soc. Rev.* **2011**, *40*, 4422–4437.

(3) Dong, L.; Feng, Y.; Wang, L.; Feng, W. Azobenzene-based solar thermal fuels: design, properties, and applications. *Chem. Soc. Rev.* **2018**, *47*, 7339–7368.

(4) Goulet-Hanssens, A.; Eisenreich, F.; Hecht, S. Enlightening Materials with Photoswitches. *Adv. Mater.* **2020**, *32*, 1905966.

(5) Santer, S. Remote control of soft nano-objects by light using azobenzene containing surfactants. *J. Phys. D: Appl. Phys.* **2017**, *51*, 013002.

(6) Bian, T.; Chu, Z.; Klajn, R. The Many Ways to Assemble Nanoparticles Using Light. *Adv. Mater.* **2020**, *32*, 1905866.

(7) Gahl, C.; Schmidt, R.; Brete, D.; McNellis, E. R.; Freyer, W.; Carley, R.; Reuter, K.; Weinelt, M. Structure and Excitonic Coupling in Self-Assembled Monolayers of Azobenzene-Functionalized Alkanethiols. *J. Am. Chem. Soc.* **2010**, *132*, 1831–1838.

(8) Pace, G.; Ferri, V.; Grave, C.; Elbing, M.; von Hänisch, C.; Zharnikov, M.; Mayor, M.; Rampi, M. A.; Samorì, P. Cooperative light-induced molecular movements of highly ordered azobenzene self-assembled monolayers. *Proc. Natl. Acad. Sci. U. S. A.* **2007**, *104*, 9937–9942.

(9) Moldt, T.; Brete, D.; Przyrembel, D.; Das, S.; Goldman, J. R.; Kundu, P. K.; Gahl, C.; Klajn, R.; Weinelt, M. Tailoring the Properties of Surface-Immobilized Azobenzenes by Monolayer Dilution and Surface Curvature. *Langmuir* **2015**, *31*, 1048–1057.

(10) Malyar, I. V.; Titov, E.; Lomadze, N.; Saalfrank, P.; Santer, S. Photoswitching of azobenzene-containing self-assembled monolayers as a tool for control over silicon surface electronic properties. *J. Chem. Phys.* **2017**, *146*, 104703.

(11) Zakrevskyy, Y.; Roxlau, J.; Brezesinski, G.; Lomadze, N.; Santer, S. Photosensitive surfactants: Micellization and interaction with DNA. *J. Chem. Phys.* **2014**, *140*, 044906.

(12) Blayo, C.; Houston, J. E.; King, S. M.; Evans, R. C. Unlocking Structure–Self-Assembly Relationships in Cationic Azobenzene Photosurfactants. *Langmuir* **2018**, *34*, 10123–10134.

(13) Titov, E.; Sharma, A.; Lomadze, N.; Saalfrank, P.; Santer, S.; Bekir, M. Photoisomerization of an Azobenzene-Containing Surfactant Within a Micelle. *ChemPhotoChem* **2021**, *5*, 926–932.

(14) Zakrevskyy, Y.; Cywinski, P.; Cywinska, M.; Paasche, J.; Lomadze, N.; Reich, O.; Löhmannsröben, H.-G.; Santer, S. Interaction of photosensitive surfactant with DNA and poly acrylic acid. *J. Chem. Phys.* **2014**, *140*, 044907.

(15) Zakrevskyy, Y.; Titov, E.; Lomadze, N.; Santer, S. Phase diagrams of DNA–photosensitive surfactant complexes: Effect of ionic strength and surfactant structure. *J. Chem. Phys.* **2014**, *141*, 164904.

(16) Kasyanenko, N.; Lysyakova, L.; Ramazanov, R.; Nesterenko, A.; Yaroshevich, I.; Titov, E.; Alexeev, G.; Lezov, A.; Unksov, I. Conformational and phase transitions in DNA—photosensitive surfactant solutions: Experiment and modeling. *Biopolymers* **2015**, *103*, 109–122.

(17) Yamauchi, M.; Yokoyama, K.; Aratani, N.; Yamada, H.; Masuo, S. Crystallization-Induced Emission of Azobenzene Derivatives. *Angew. Chem. Int. Ed.* **2019**, *58*, 14173–14178.

(18) Hermann, D.; Schwartz, H. A.; Ruschewitz, U. Crystal Structures of Z and E ortho-Tetrafluoroazobenzene. *ChemistrySelect* **2017**, *2*, 11846–11852.

(19) Koshima, H.; Ojima, N.; Uchimoto, H. Mechanical Motion of Azobenzene Crystals upon Photoirradiation. *J. Am. Chem. Soc.* **2009**, *131*, 6890–6891.

(20) Davydov, A. S. The theory of molecular excitons. *Soviet Physics Uspekhi* **1964**, *7*, 145–178.

(21) Kasha, M.; Rawls, H. R.; El-Bayoumi, M. A. The exciton model in molecular spectroscopy. *Pure Appl. Chem.* **1965**, *11*, 371–392.

(22) Valley, D. T.; Onstott, M.; Malyk, S.; Benderskii, A. V. Steric Hindrance of Photoswitching in Self-Assembled Monolayers of Azobenzene and Alkane Thiols. *Langmuir* **2013**, *29*, 11623–11631.

(23) Utecht, M.; Klamroth, T.; Saalfrank, P. Optical absorption and excitonic coupling in azobenzenes forming self-assembled monolayers: a study based on density functional theory. *Phys. Chem. Chem. Phys.* **2011**, *13*, 21608–21614.

(24) Titov, E.; Saalfrank, P. Exciton Splitting of Adsorbed and Free 4-Nitroazobenzene Dimers: A Quantum Chemical Study. *J. Phys. Chem. A* **2016**, *120*, 3055–3070.

(25) Cocchi, C.; Draxl, C. Understanding the effects of packing and chemical terminations on the optical excitations of azobenzene-functionalized self-assembled monolayers. *J. Phys.: Condens. Matter* **2017**, *29*, 394005.

(26) Titov, E.; Beqiraj, A. Exciton States of Azobenzene Aggregates: A First-Principles Study. *Adv. Theory Simul.* **2023**, 2200907.

(27) Floß, G.; Granucci, G.; Saalfrank, P. Surface hopping dynamics of direct trans $\rightarrow$ cis photoswitching of an azobenzene derivative in constrained adsorbate geometries. *J. Chem. Phys.* **2012**, *137*, 234701.

(28) Benassi, E.; Granucci, G.; Persico, M.; Corni, S. Can Azobenzene Photoisomerize When Chemisorbed on a Gold Surface? An Analysis of Steric Effects Based on Nonadiabatic Dynamics Simulations. *J. Phys. Chem. C* **2015**, *119*, 5962–5974.

(29) Cantatore, V.; Granucci, G.; Rousseau, G.; Padula, G.; Persico, M. Photoisomerization of Self-Assembled Monolayers of Azobiphenyls: Simulations Highlight the Role of Packing and Defects. *J. Phys. Chem. Lett.* **2016**, *7*, 4027–4031.

(30) Mondal, P.; Granucci, G.; Rastädter, D.; Persico, M.; Burghardt, I. Azobenzene as a photoregulator covalently attached to RNA: a quantum mechanics/molecular mechanics-surface hopping dynamics study. *Chem. Sci.* **2018**, *9*, 4671–4681.

(31) Osella, S.; Granucci, G.; Persico, M.; Knippenberg, S. Dual photoisomerization mechanism of azobenzene embedded in a lipid membrane. *J. Mater. Chem. B* **2023**, *11*, 2518–2529.

(32) Benassi, E.; Corni, S. Exciton Transfer of Azobenzene Derivatives in Self-Assembled Monolayers. *J. Phys. Chem. C* **2013**, *117*, 25026–25041.

(33) Titov, E.; Granucci, G.; Götze, J. P.; Persico, M.; Saalfrank, P. Dynamics of Azobenzene Dimer Photoisomerization: Electronic and Steric Effects. *J. Phys. Chem. Lett.* **2016**, *7*, 3591–3596.

(34) Rietze, C.; Titov, E.; Granucci, G.; Saalfrank, P. Surface Hopping Dynamics for Azobenzene Photoisomerization: Effects of Packing Density on Surfaces, Fluorination, and Excitation Wavelength. *J. Phys. Chem. C* **2020**, *124*, 26287–26295.

(35) Titov, E. Effect of conformational disorder on exciton states of an azobenzene aggregate. *Phys. Chem. Chem. Phys.* **2022**, *24*, 24002–24006.

(36) Plasser, F.; Granucci, G.; Pittner, J.; Barbatti, M.; Persico, M.; Lischka, H. Surface hopping dynamics using a locally diabatic formalism: Charge transfer in the ethylene dimer cation and excited state dynamics in the 2-pyridone dimer. *J. Chem. Phys.* **2012**, *137*, 22A514.

(37) Fernandez-Alberti, S.; Roitberg, A. E.; Kleiman, V. D.; Nelson, T.; Tretiak, S. Shishiodoshi unidirectional energy transfer mechanism in phenylene ethynylene dendrimers. *J. Chem. Phys.* **2012**, *137*, 22A526.

(38) Galindo, J. F.; Atas, E.; Altan, A.; Kuroda, D. G.; Fernandez-Alberti, S.; Tretiak, S.; Roitberg, A. E.; Kleiman, V. D. Dynamics of Energy Transfer in a Conjugated Dendrimer Driven by Ultrafast Localization of Excitations. *J. Am. Chem. Soc.* **2015**, *137*, 11637–11644.

(39) Nelson, T.; Fernandez-Alberti, S.; Roitberg, A. E.; Tretiak, S. Electronic Delocalization, Vibrational Dynamics, and Energy Transfer in Organic Chromophores. *J. Phys. Chem. Lett.* **2017**, *8*, 3020–3031.

(40) Titov, E.; Humeniuk, A.; Mitrić, R. Exciton localization in excited-state dynamics of a tetracene trimer: a surface hopping LC-TDDFTB study. *Phys. Chem. Chem. Phys.* **2018**, *20*, 25995–26007.

(41) Titov, E.; Kopp, T.; Hoche, J.; Humeniuk, A.; Mitrić, R. (De)localization dynamics of molecular excitons: comparison of mixed quantum-classical and fully quantum treatments. *Phys. Chem. Chem. Phys.* **2022**, *24*, 12136–12148.

(42) Stojanović, L.; Aziz, S. G.; Hilal, R. H.; Plasser, F.; Niehaus, T. A.; Barbatti, M. Nonadiabatic Dynamics of Cycloparaphenylenes with TD-DFTB Surface Hopping. *J. Chem. Theory Comput.* **2017**, *13*, 5846–5860.

(43) Wang, J.; Huang, J.; Du, L.; Lan, Z. Photoinduced Ultrafast Intramolecular Excited-State Energy Transfer in the Silylene-Bridged Biphenyl and Stilbene (SBS) System: A Nonadiabatic Dynamics Point of View. *J. Phys. Chem. A* **2015**, *119*, 6937–6948.

(44) Zhang, S.; Zeng, Y.-P.; Wan, X.-J.; Xu, D.-H.; Liu, X.-Y.; Cui, G.; Li, L. Ultrafast exciton delocalization and localization dynamics of a perylene bisimide quadruple π-stack: a nonadiabatic dynamics simulation. *Phys. Chem. Chem. Phys.* **2022**, *24*, 7293–7302.

(45) Sangiogo Gil, E.; Granucci, G.; Persico, M. Surface Hopping Dynamics with the Frenkel Exciton Model in a Semiempirical Framework. *J. Chem. Theory Comput.* **2021**, *17*, 7373–7383.

(46) Sangiogo Gil, E.; Persico, M.; Granucci, G. Frenkel exciton photodynamics of self-assembled monolayers of azobiphenyls. *J. Chem. Phys.* **2022**, *157*, 161101.

(47) Granucci, G.; Toniolo, A. Molecular gradients for semiempirical CI wavefunctions with floating occupation molecular orbitals. *Chem. Phys. Lett.* **2000**, *325*, 79–85.

(48) Dewar, M. J. S.; Zoebisch, E. G.; Healy, E. F.; Stewart, J. J. P. Development and use of quantum mechanical molecular models. 76. AM1: a new general purpose quantum mechanical molecular model. *J. Am. Chem. Soc.* **1985**, *107*, 3902–3909.

(49) Cusati, T.; Granucci, G.; Martínez-Núñez, E.; Martini, F.; Persico, M.; Vázquez, S. Semiempirical Hamiltonian for Simulation of Azobenzene Photochemistry. *J. Phys. Chem. A* **2012**, *116*, 98–110.

(50) Accomasso, D.; Granucci, G.; Persico, M. Singlet fission in covalent dimers of methylene-locked 1,3-diphenyl-isobenzofuran: semiclassical simulations of nonadiabatic dynamics. *J. Mater. Chem. A* **2021**, *9*, 21897–21909.

(51) The vdW parameters are taken from the oplsaa.prm file of TINKER 6.1 distribution. These parameters, in turn, are from "OPLS All-Atom Parameters for Organic Molecules, Ions, Peptides & Nucleic Acids, July 2008" as provided by W. L. Jorgensen, Yale University during June 2009.

(52) Tully, J. C. Molecular dynamics with electronic transitions. *J. Chem. Phys.* **1990**, *93*, 1061–1071.

(53) Granucci, G.; Persico, M.; Toniolo, A. Direct semiclassical simulation of photochemical processes with semiempirical wave functions. *J. Chem. Phys.* **2001**, *114*, 10608–10615.

(54) Granucci, G.; Persico, M. Critical appraisal of the fewest switches algorithm for surface hopping. *J. Chem. Phys.* **2007**, *126*, 134114.

(55) McWeeny, R. Some Recent Advances in Density Matrix Theory. *Rev. Mod. Phys.* **1960**, *32*, 335–369.

(56) Tretiak, S.; Mukamel, S. Density Matrix Analysis and Simulation of Electronic Excitations in Conjugated and Aggregated Molecules. *Chem. Rev.* **2002**, *102*, 3171–3212.

(57) Plasser, F.; Lischka, H. Analysis of Excitonic and Charge Transfer Interactions from Quantum Chemical Calculations. *J. Chem. Theory Comput.* **2012**, *8*, 2777–2789.

(58) Titov, E. On the Low-Lying Electronically Excited States of Azobenzene Dimers: Transition Density Matrix Analysis. *Molecules* **2021**, *26*, 4245.

(59) Nogueira, J. J.; Plasser, F.; González, L. Electronic delocalization, charge transfer and hypochromism in the UV absorption spectrum of polyadenine unravelled by multiscale computations and quantitative wavefunction analysis. *Chem. Sci.* **2017**, *8*, 5682–5691.

(60) Ondarse-Alvarez, D.; Kömürlü, S.; Roitberg, A. E.; Pierdominici-Sottile, G.; Tretiak, S.; Fernandez-Alberti, S.; Kleiman, V. D. Ultrafast electronic energy relaxation in a conjugated dendrimer leading to inter-branch energy redistribution. *Phys. Chem. Chem. Phys.* **2016**, *18*, 25080–25089.

(61) Stewart, J. J. P. MOPAC 2002, Fujitsu Ltd., Tokyo, Japan.

(62) Rackers, J. A.; Wang, Z.; Lu, C.; Laury, M. L.; Lagardère, L.; Schnieders, M. J.; Piquemal, J.-P.; Ren, P.; Ponder, J. W. Tinker 8: Software Tools for Molecular Design. *J. Chem. Theory Comput.* **2018**, *14*, 5273–5289.

(63) Åke Andersson, J.; Petterson, R.; Tegnér, L. Flash photolysis experiments in the vapour phase at elevated temperatures I: spectra of azobenzene and the kinetics of its thermal cis-trans isomerization. *J. Photochem.* **1982**, *20*, 17–32.

(64) Cusati, T.; Granucci, G.; Persico, M.; Spighi, G. Oscillator strength and polarization of the forbidden $n \rightarrow \pi^*$ band of trans-azobenzene: A computational study. *J. Chem. Phys.* **2008**, *128*, 194312.

(65) Ciminelli, C.; Granucci, G.; Persico, M. The Photoisomerization Mechanism of Azobenzene: A Semiclassical Simulation of Nonadiabatic Dynamics. *Chem. Eur. J.* **2004**, *10*, 2327–2341.

(66) Cantatore, V.; Granucci, G.; Persico, M. Simulation of the $\pi \rightarrow \pi^*$ photodynamics of azobenzene: Decoherence and solvent effects. *Comput. Theor. Chem.* **2014**, *1040-1041*, 126–135.

(67) Floß, G.; Saalfrank, P. The Photoinduced E $\rightarrow$ Z Isomerization of Bisazobenzenes: A Surface Hopping Molecular Dynamics Study. *J. Phys. Chem. A* **2015**, *119*, 5026–5037.

(68) Xu, C.; Yu, L.; Gu, F. L.; Zhu, C. Probing the $\pi \rightarrow \pi^*$ photoisomerization mechanism of trans-azobenzene by multi-state ab initio on-the-fly trajectory dynamics simulations. *Phys. Chem. Chem. Phys.* **2018**, *20*, 23885–23897.

(69) Yu, J. K.; Bannwarth, C.; Liang, R.; Hohenstein, E. G.; Martínez, T. J. Nonadiabatic Dynamics Simulation of the Wavelength-Dependent Photochemistry of Azobenzene Excited to the nπ^* and $\pi\pi^*$ Excited States. *J. Am. Chem. Soc.* **2020**, *142*, 20680–20690.

(70) Ladányi, V.; Dvořák, P.; Al Anshori, J.; Vetráková, L.; Wirz, J.; Heger, D. Azobenzene photoisomerization quantum yields in methanol redetermined. *Photochem. Photobiol. Sci.* **2017**, *16*, 1757–1761.